Electronic Supplementary Information (ESI)

Vertically Aligned $BaTiO_3$ Nanowire Arrays for Energy Harvesting

Aneesh Koka,[a] Zhi Zhou[b] and Henry A. Sodano*[a,b]

[a]*Mechanical and Aerospace Engineering, University of Florida, Gainesville, Florida 32611, USA*

[b]*Materials Science and Engineering, University of Florida, Gainesville, Florida 32611, USA*

[*]*E-mail: hsodano@ufl.edu*

Growth approach of vertically aligned $BaTiO_3$ nanowire arrays.

A two-step hydrothermal growth approach is used to synthesize aligned $BaTiO_3$ nanowire (NW) arrays on fluorine doped tin oxide (FTO) glass that is inexpensive. Previous hydrothermal methods used for the formation of $BaTiO_3$ nanostructures,[1-3] have shown the synthesis to be highly dependent on the type of precursor used as it must accept barium ion diffusion for structural transformation while preserving the precursors' shape. Owing to this reason, we first hydrothermally synthesized vertically aligned titanium dioxide NW arrays on an FTO glass, and used them as precursors for conversion to $BaTiO_3$ while preserving the NW array form.[4, 5] The titanium dioxide NW arrays of length ~1 μm and diameter of ~90 nm remain firmly attached to the conductive FTO layer following the first hydrothermal reaction and even maintain their NW form when ultra-sonicated thereby substantiating their excellent adherence and rigidity. The as-synthesized titanium dioxide NW arrays grown on FTO glass are of low density to allow conversion to $BaTiO_3$ NW arrays through the reaction of Ba^{2+} ions with the rutile lattice.

Consequently, these titanium dioxide NW arrays were utilized as precursors and converted to $BaTiO_3$ NW arrays using a second hydrothermal reaction in aqueous barium hydroxide octahydrate solution containing Ba^{2+} ions at temperatures between 150-250ºC. In order to effectively convert the nanowire arrays, the pH value of the solution and reaction time must be carefully controlled to prevent etching of FTO coated glass substrate and also to ensure the morphology of the template arrays is maintained. During this second hydrothermal reaction, the TiO_2 is dissolved in the solution to form $Ti(OH)_4$, which subsequently reacts with the Ba ions and forms a layer of $BaTiO_3$ on the surface of the TiO_2. Subsequently with increasing reaction time, the $BaTiO_3$ crystals evolve and eventually convert completely from single crystal TiO_2 to single crystal $BaTiO_3$. A detailed characterization was performed using the X-ray diffractometer

(XRD) to identify all the materials' crystal structure used for synthesizing $BaTiO_3$ NW arrays starting from the initial FTO glass substrate to the rutile titanium dioxide nanowire precursor (Supplementary Fig. S1). The XRD pattern of titanium dioxide used as precursors showed a majority of the peaks to match with rutile titanium dioxide (JCPDS No. 76-1940).

Fabrication and Performance Evaluation of $BaTiO_3$ NW based NEMS energy harvester.

The $BaTiO_3$ NW based NEMS energy harvester is fabricated with a conductive FTO layer on a glass substrate as the bottom electrode and indium beam as the top electrode with as-synthesized $BaTiO_3$ NW arrays in a sandwich configuration. The as-fabricated $BaTiO_3$ energy harvester is then polled under high electric field (120 kV/cm) to ensure the electric dipoles align in the direction normal to the two electrodes. The poled functional $BaTiO_3$ NW NEMS energy harvester is then mounted on a miniature permanent magnet shaker with a reference shear accelerometer (PCB352C22) mounted beside it to measure the input base acceleration supplied to it as shown in Supplementary Fig. S2. A faraday cage surrounds the entire setup to attenuate the extrinsic interference noise from environment.

The capacitance and the impedance consisting of series resistance (R_S) and the reactance ($X_C = 1/(j\omega C)$) of the $BaTiO_3$ NEMS energy harvester (Supplementary Fig. S3a) is measured using a high precision LCR meter (Agilent E4980A). The open circuit voltage (V_{OC}) and the short circuit current (I_{SC}) measurements are performed using a unity gain voltage follower (LTC6240CS8)[6] and the high speed electrometer (Keithley 6514) respectively. The frequency response function (FRF) characterization is performed to locate the resonant magnitude peak of the energy harvester by exciting with burst chirp and white Gaussian noise signals that have a flat spectral density in the frequency range of up to 1 kHz as shown in Supplementary Fig. S4. The V_{OC} response and I_{SC} response from $BaTiO_3$ energy harvester when excited with burst chirp signal is shown in Supplementary Fig. S5. AC power is evaluated by exciting the energy harvester with a 1g root mean square (RMS) sinusoidal acceleration input at the resonant frequency and then measuring the RMS voltage (V_L) across the load resistors (R_L). Maximum AC power is obtained at the optimal load resistor that is close to the source impedance as per maximum power transfer theorem. The power density is calculated from the ratio of AC power to the volume. For the as-fabricated $BaTiO_3$ NEMS energy harvester with resonant frequency at 160 Hz, the peak AC power and peak power density is determined to be ~125.5 pW and ~6.27 μW/cc respectively at the optimal load resistor of 120 MΩ from base acceleration input of 1g RMS.

Fabrication and Performance Evaluation of ZnO NW based NEMS energy harvester.

The ZnO NW NEMS energy harvester is fabricated in the similar procedure as $BaTiO_3$ energy harvester with the indium beam as top electrode and conductive FTO layer as bottom electrode since the ZnO NW arrays were also synthesized on a conductive FTO glass substrate by solution growth approach at low temperature.[7-9] The capacitance and impedance measurements are performed using Agilent E4980A LCR meter which validates the presence of capacitive contact (Supplementary Fig. S3b). Similar measurements of V_{OC} and I_{SC} are performed and FRF characterization is done to locate the resonant magnitude peak (see Supplementary Fig.S5a-b for V_{OC} and I_{SC} response to burst chirp input used for FRF characterization). For the ZnO NEMS energy harvester with a resonant peak at 190 Hz, the peak AC power and power density is calculated to be ~8 pW and ~0.4 μW/cc respectively at the optimal load resistor of 50 MΩ shown clearly in Supplementary Fig. S5c. The voltage (V_L) measured across the 50 MΩ load resistor with an RMS value of ~20.2 mV provides the peak power density (Supplementary Fig. S5d). The area of the indium beam over the NW array is dimensioned to be 5 mm X 4 mm for both the $BaTiO_3$ and ZnO NEMS energy harvester for ease of comparison of power density and both were excited with the same base acceleration of 1g RMS sine wave (see Supplementary Table 1 for properties of NEMS energy harvester). Therefore, experimental validation of the superior power density from ferroelectric $BaTiO_3$ NW arrays is demonstrated which is ~16 times greater than the peak power density of the semi-conductive ZnO NW arrays.

Switching polarity test on $BaTiO_3$ NW NEMS energy harvester.

To confirm the measured response is from the novel $BaTiO_3$ NW NEMS energy harvester, a switching polarity test is performed on the energy harvester to rule out any measurement artifacts such as capacitive coupling which does not reverse their polarity when the connection is switched from forward to reverse mode.[10, 11] The voltage response to 20 Hz pulse input excitation is measured by forward connecting to the voltage follower and when switched to backward connection, the measured response is observed to be reversed in polarity thereby confirming that the measured signals from the $BaTiO_3$ NEMS is generated by the nanowires. The polarity of the voltage response from the poled $BaTiO_3$ NEMS energy harvester should be same under the same mechanical deformation so a reverse in polarity can be witnessed when the

connection is reversed to the measurement system (voltage buffer amplifier) as shown in Supplementary Fig. S7.

Table S1. Properties of NEMS Energy Harvester

Property	Value
Dimension of indium beam in $BaTiO_3$ NW NEMS Energy Harvester (length x width x thickness)	12 mm x 4 mm x 0.127 mm
Dimension of indium beam in ZnO NW NEMS Energy Harvester (length x width x thickness)	12 mm x 4 mm x 0.127 mm
Dimension of Indium above NW array	5 mm X 4mm
Source Capacitance (C_p) of $BaTiO_3$ NW NEMS Energy Harvester	8.21 pF
Source Impedance ($Z_s = 1/(\omega_n C_p)$) of $BaTiO_3$ NW NEMS Energy Harvester with f_n = 160 Hz	~121 MΩ
Source Capacitance (C_p) of ZnO NW NEMS Energy Harvester	8.72 pF
Source Impedance ($Z_s = 1/(\omega_n C_p)$) of ZnO NW NEMS Energy Harvester with f_n = 190 Hz	~96 MΩ

Supplementary Figures:

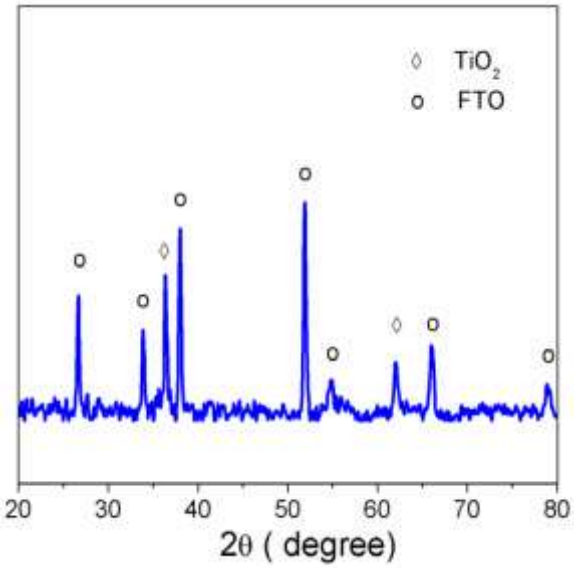

Fig. S1 Characterization of precursor TiO_2 NW arrays. Rutile TiO_2 NW arrays grown on FTO glass analyzed using X-ray diffraction (XRD) (rutile TiO_2 JCPDS No. 76-1940).

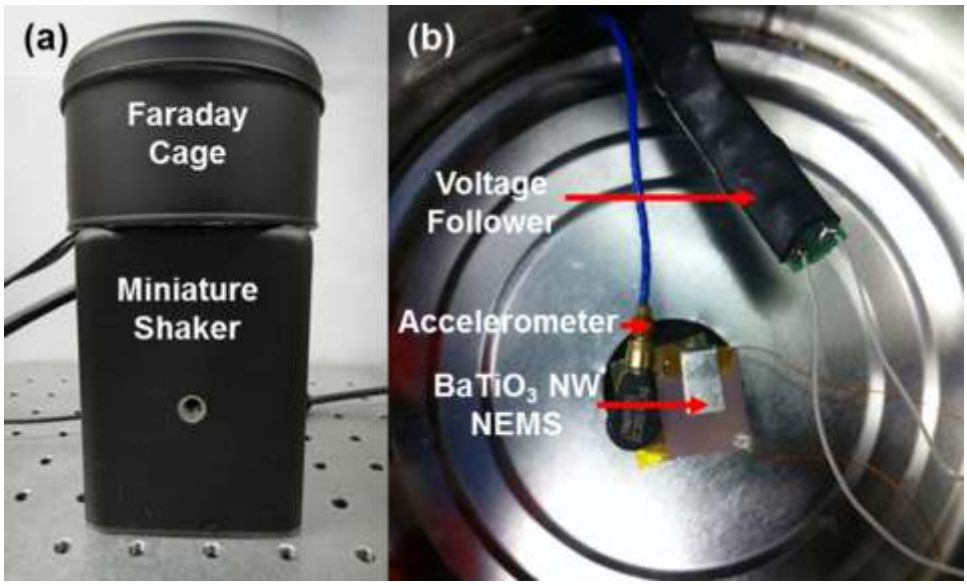

Fig. S2 Experimental setup for characterization of NW NEMS energy harvester. (a) Image of the setup showing the miniature permanent magnet shaken used to generate the base vibration and the grounded faraday cage surrounding the NW NEMS energy harvester used as an extrinsic noise shield. (b) Photographic image showing the arrangement inside the faraday cage.

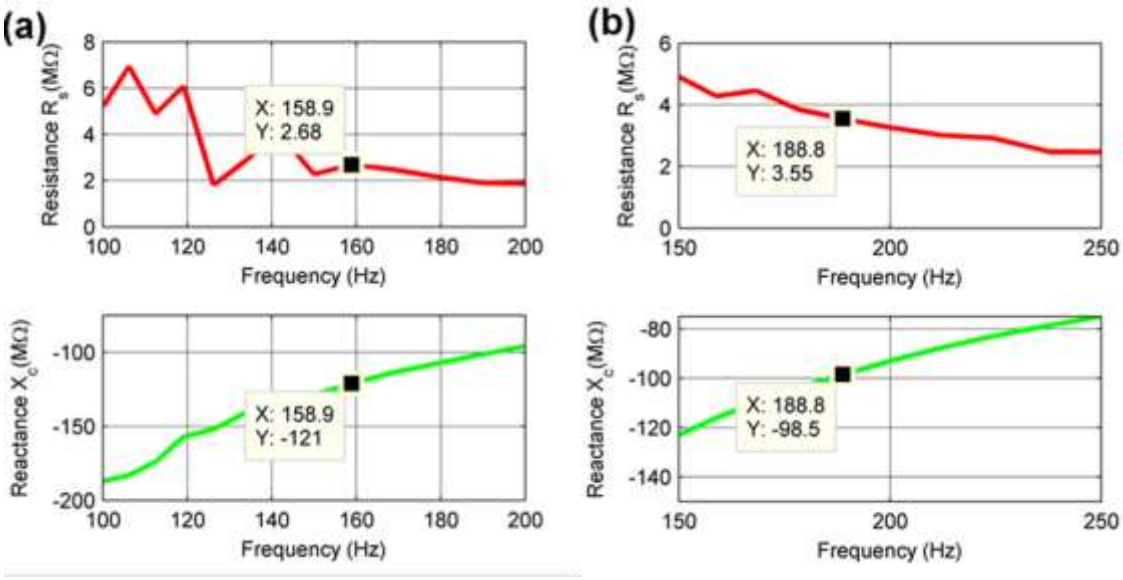

Fig. S3 Impedance Measurement. (a) Resistance (R_s) and Reactance (X_c) of $BaTiO_3$ NW NEMS energy harvester used for AC power characterization with the data points showing the values close to resonant frequency (~160 Hz). (b) Resistance (R_s) and Reactance (X_c) of ZnO NW NEMS energy harvester used for AC power characterization with the data points showing the values near resonant frequency (~190 Hz).

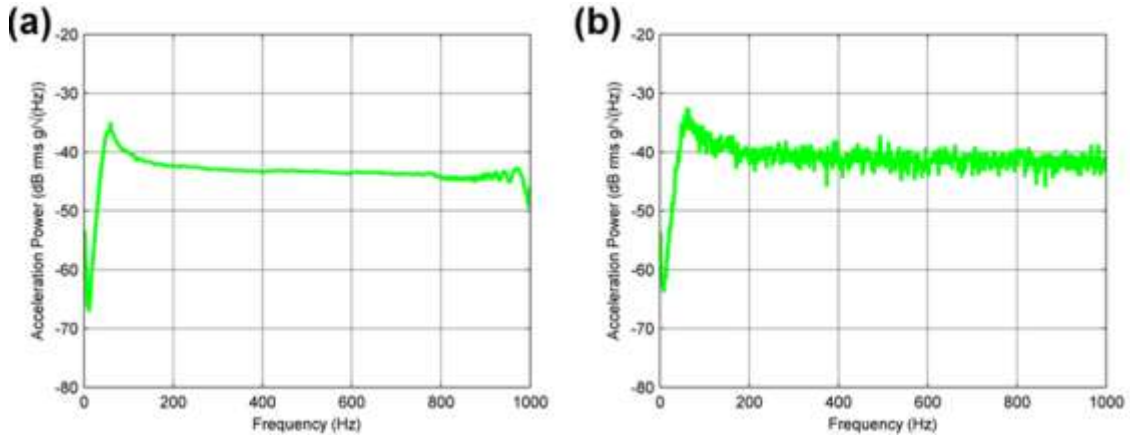

Fig. S4 Spectral density of input signal for frequency response function (FRF) characterization. (a) Spectral Density of Burst Chirp. (b) Spectral Density of white Gaussian noise.

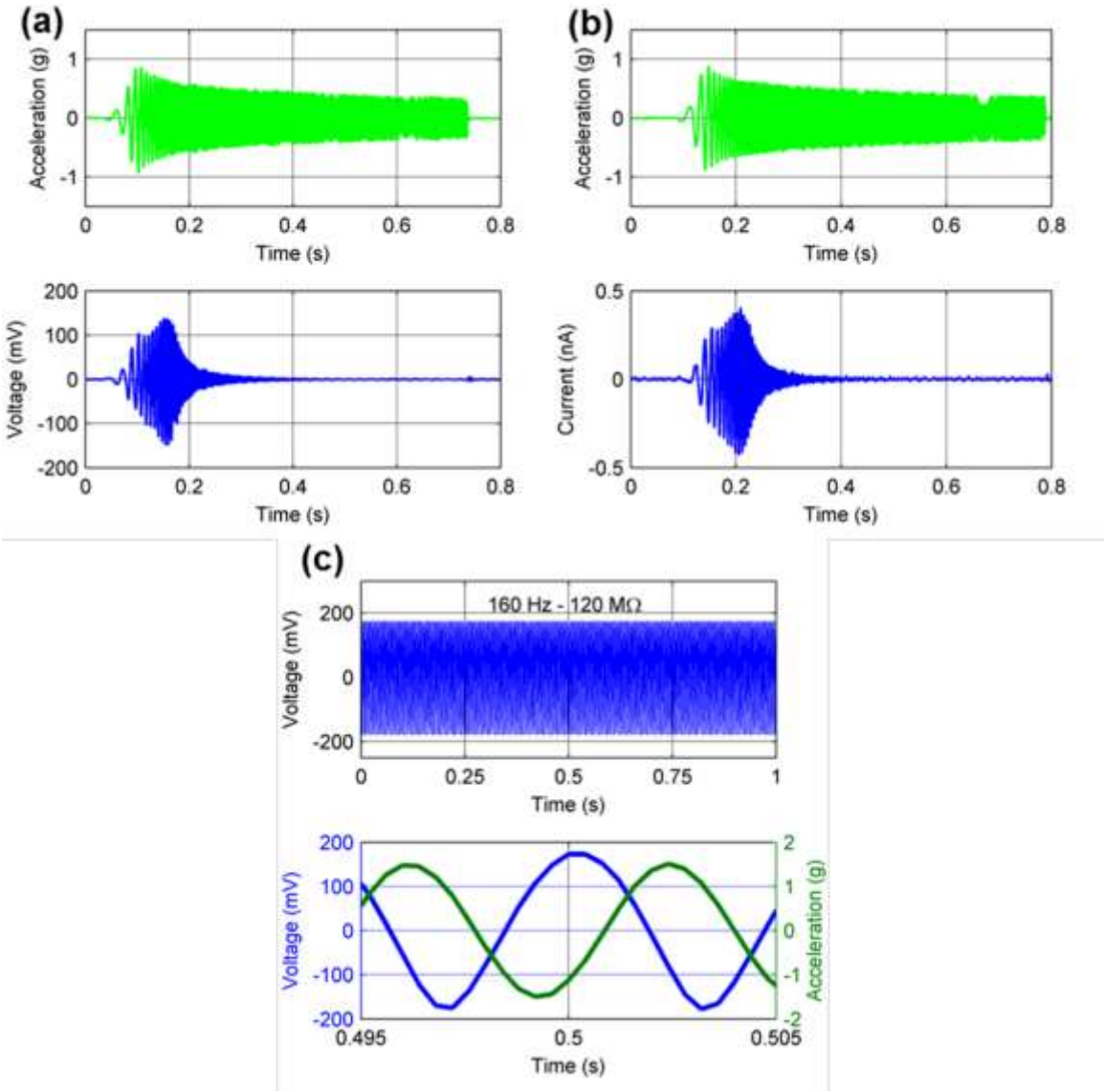

Fig. S5 Characterization of $BaTiO_3$ NW NEMS energy harvester excited with burst chirp. (a) Voltage response to burst chirp used for V_{OC} FRF characterization. (b) Short circuit current response to burst chirp used for I_{SC} FRF characterization. (c) Voltage (V_L) measured across 120 MΩ optimal load resistor (R_L) at resonant frequency with an RMS value of ~123 mV from $BaTiO_3$ NW NEMS energy harvester with the detailed shape of both the voltage and acceleration in the bottom panel.

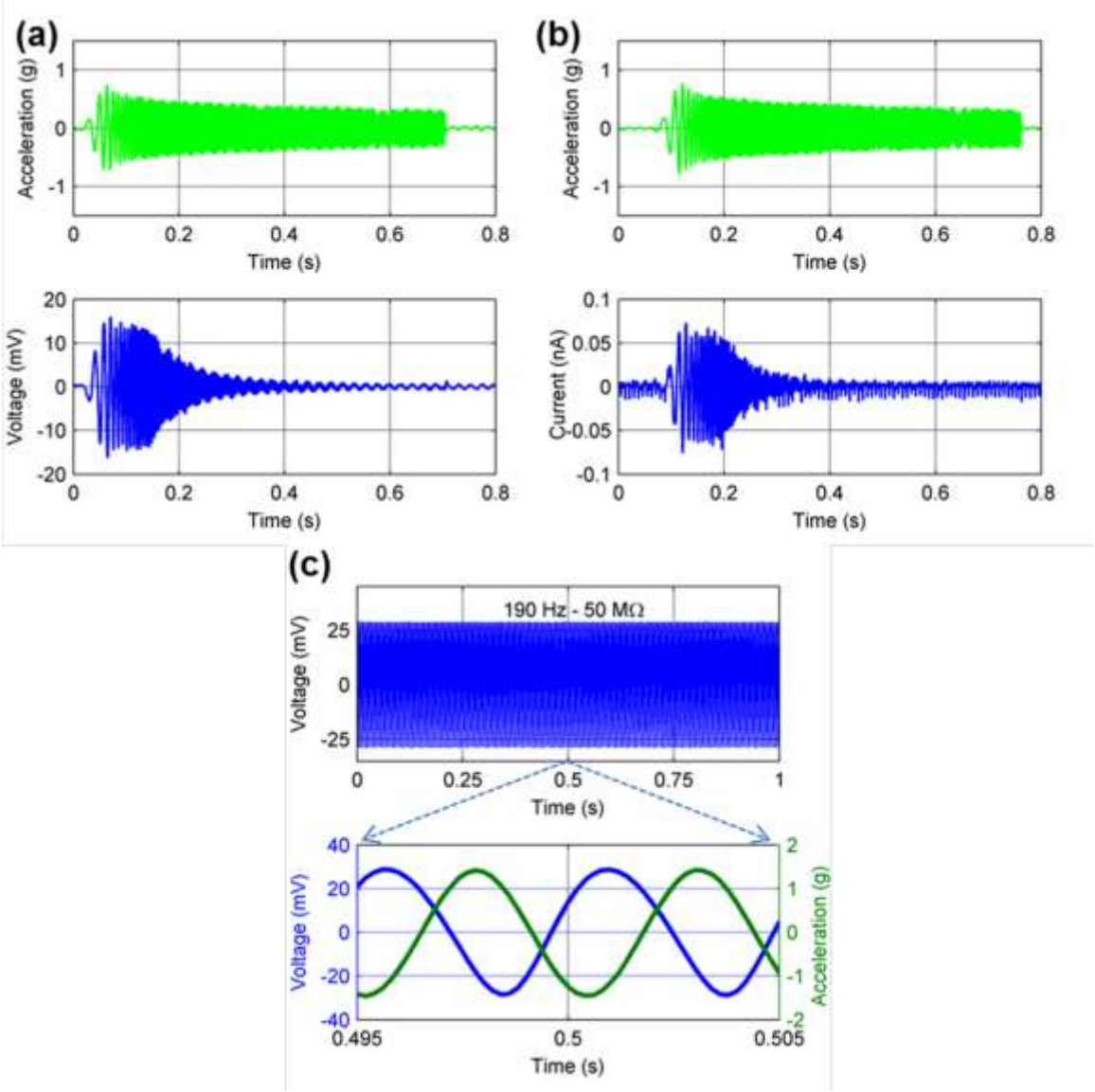

Fig. S6 Characterization of ZnO NW NEMS energy harvester. (a) Voltage response to burst chirp used for V_{OC} FRF characterization for ZnO NW NEMS energy harvester. (b) Short circuit current response to burst chirp used for I_{SC} FRF characterization for ZnO NW NEMS energy harvester. (c) AC power and power density from ZnO NW NEMS across several load resistors with the peak AC power and power density of ~8 pW and ~0.4 μW/cc respectively at 50 MΩ optimal load resistor (R_L). (d) Voltage (V_L) measured across the 50 MΩ optimal load resistor (R_L) with RMS value of 20.2 mV from the ZnO NW NEMS energy harvester with the detailed shape of both the voltage and acceleration in the bottom panel.

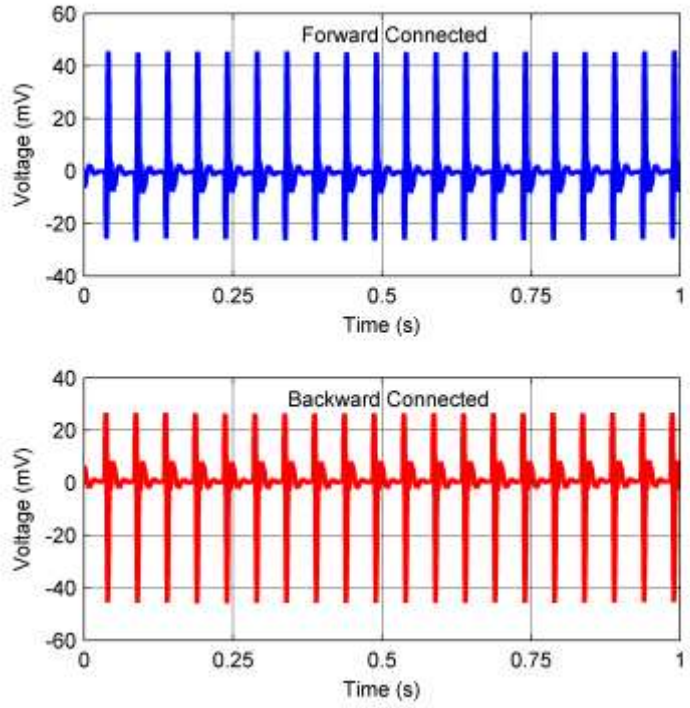

Fig. S7 Switching polarity test of $BaTiO_3$ NW NEMS energy harvester. The $BaTiO_3$ NW NEMS is excited with pulse input at 20 Hz frequency when forward connected and backward connected to the voltage follower to demonstrate the reversing voltage signal which confirms that the measured response is generated by $BaTiO_3$ NW arrays.

Additional References

1 Y. Yang, X. Wang, C. Sun and L. Li, *Nanotechnology*, 2009, **20**, 055709.

2 D. Chen, H. Zhang, R. Chen, X. Deng, J. Li, G. Zhang and L. Wang, *Phys. Status Solidi. A.*, 2012, **209**, 714-717.

3 F. Maxim, P. M. Vilarinho, P. Ferreira, I. M. Reaney and I. Levin, *Cryst. Growth Des.*, 2011, **11**, 3358-3365.

4 B. Liu and E. S. Aydil, *J. Am. Chem. Soc.*, 2009, **131**, 3985-3990.

5 A. Kumar, A. R. Madaria and C. Zhou, *J. Phys. Chem. C.*, 2010, **114**, 7787-7792.

6 'Linear Technology', *LTC6240/LTC6241/LTC6242 Single/Dual/Quad 18MHz, Low noise, Rail-to-Rail Output, CMOS Op Amps*, 2011.

7 L. E. Greene, B. D. Yuhas, M. Law, D. Zitoun and P. Yang, *Inorg. Chem.*, 2006, **45**, 7535-7543.

8 U. Galan, Y. Lin, G. J. Ehlert and H. A. Sodano, *Composites Sci. Technol.*, 2011, **71**, 946-954.

9 C. Xu and D. Gao, *J. Phys. Chem. C.*, 2012, **116**, 7236-7241.

10 R. Yang, Y. Qin, C. Li, L. Dai and Z. L. Wang, *Appl. Phys. Lett.*, 2009, **94**, 022905-3.

11 J. Chang, M. Dommer, C. Chang and L. Lin, *Nano Energy*, 2012, **1**, 356-371.